ESTEC

European Space Research
and Technology Centre
Keplerlaan 1
2201 AZ Noordwijk
The Netherlands
www.esa.int

PERFORMANCE REPORT

The spectral calibration of JWST/NIRSpec: accuracy of the instrument model for the OTIS test cycle

Prepared by G. Giardino and N. Luetzgendorf

Reference ESA-JWST-SCI-NRS-RP-2017-004
Issue/Revision 1.0
Date of Issue January 15, 2018
Status Released

APPROVAL

Title The spectral calibration of JWST/NIRSpec: accuracy of the instrument model for the OTIS test cycle	
Issue Number 1	**Revision Number** 0
Author G. Giardino and N. Luetzgendorf	**Date** January 15, 2018
Approved by	**Date of Approval**
M.Sirianni	January 15, 2018

CHANGE LOG

Reason for change	Issue Nr.	Revision Number	Date

CHANGE RECORD

Issue Number 1	Revision Number 0		
Reason for change	**Date**	**Pages**	**Paragraph(s)**

DISTRIBUTION

Name/Organisational Unit
SCI-ODJ
ESTEC

Contents

1 INTRODUCTION

The NIRSpec parametric model is the backbone of the spatial and wavelength calibration of the spectra obtained with all the instrument spectroscopic modes: Fixed Slits, Multi-object spectroscopy (MOS), and Integral Field Unit (IFU). Although it was originally developed to make predictive "forward" simulations of NIRSpec data, once properly calibrated, the parametric model naturally also provides the geometrical transformations to i) enable the extraction of the spectra from NIRSpec images and to ii) aid the required computations for the on-board target acquisition procedure.

We have developed a procedure that uses the calibration data acquired for a limited subset of the NIRSpec modes - and in particular only 1.5% of NIRSpec's a quarter of a million slits - to fine-tune the parameters of the instrument model and we have demonstrated (Dorner et al. 2016) that the model can be calibrated with an accuracy well within requirements, using data acquired during NIRSpec Performance Verification and Calibration campaign, undertaken at the IABG testing facilities in Germany in 2013 (Birkmann et al. 2012).

Early in 2015 the Micro Shutter Assembly (MSA) and the Focal Plane Assembly (FPA) of NIRSpec were replaced. The quadrants of the new MSA had a smaller number of stuck closed shutters and the new FPA unit featured two new H2RG detectors, not affected by the performance degradation problem of the older model Rauscher et al. (2014). Therefore, the instrument model had to be updated to reflect the changes in the optical geometry of these elements as well as the overall instrument alignment. A new extensive set of imaging and spectral reference data was acquired, during the ISIM-CV3 cycle of cryogenic tests that NIRSpec underwent together with the other three scientific instruments of JWST integrated in the Integrated Scientific Instrument Module (ISIM) at NASA GSFC (Kimble et al. 2016), over the winter 2015-2016. Using those data, the instrument model was re-calibrated, also in this case, to an accuracy well within requirements (Giardino & Lützgendorf 2016; Giardino et al. 2016).

In the summer of 2017, NASA performed a cycle of cryogenic tests of ISIM integrated with the Optical Element (OTE): the OTIS (from OTE + ISIM $\rightarrow$ OTIS) test campaign. In between the two test campaigns, ISIM had to be handled for integration and the OTIS system underwent qualification-level acoustics and vibration tests, as well as transportation from GSFC (Maryland) to JSC (Texas). This could have caused changes in some of the alignment parameters of the NIRSpec instrument model. During the OTIS campaign, therefore we acquired a new (smaller) set of data and performed a new optimization of the parametric model.

In this document, we summarize the procedure that we followed to optimize the value of the model parameters using these recently-acquired data and present the results in terms of the accuracy of the model spatial and wavelength calibration.

2 THE OPTIMIZATION OF NIRSPEC PARAMETRIC MODEL

Fig. 1 provides a schematic depiction of NIRSpec optical design and identifies its main optical elements, which are encapsulated in the NIRSpec parametric model. These are: the FORE optics which re-image the telescope image plane (OTEIP = optical telescope element image plane) onto the slit plane, the Filter Wheel Assembly (FWA) located in the pupil of the FORE, the MSA in the slit-plane, the collimator optics (COL) that project the light from the slits onto the Grating Wheel Assembly (GWA), the disperser elements (gratings and prism) and the mirror housed in the GWA, the camera optics (CAM), and the FPA. The IFU entrance aperture is located in the MSA plane; the IFU optics are split into an IFU FORE part, which re-images and re-scales the MSA plane onto the slicer, and an IFU POST part, which picks up the 30 image parts and creates a virtual image for each slice at the MSA plane (virtual slits).

There are two types of components in the NIRSpec parametric model: the parameterization of the coordinate transforms between the principal optical planes (here COL, IFU FORE, IFU POST, and CAM) and the geometrical description of the key plane elements (MSA, IFU slicer, GWA, and FPA). The coordinate transforms consist of a paraxial transform between the principal planes, plus two fifth-order, two-dimensional polynomial that model

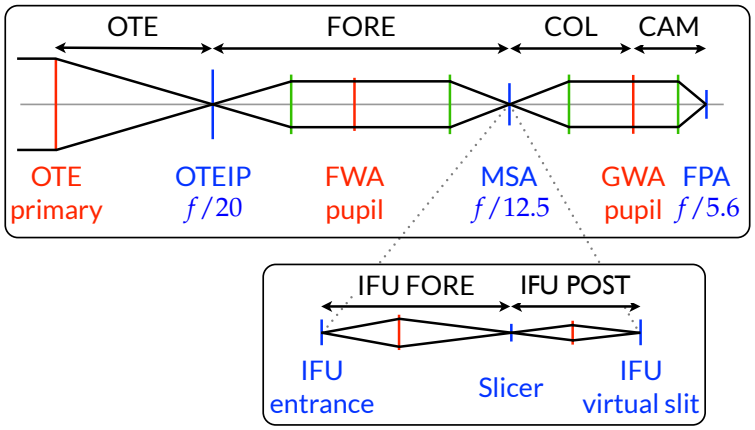

Figure 1: Paraxial layout of the JWST telescope and NIRSpec optical train with elements at principal planes, and the insert for the IFU case. Focal planes are blue, pupil planes red. All these elements are encapsulated in the NIRSpec parametric model.

the distortions in x and y – see Giardino (2013) and Dorner et al. (2016) for a detailed description of the model elements and the list of free parameters (that are more than 300 in total). Although, the parametric model encapsulates all of the main optical elements identified in Fig. 1, the work presented here is limited to the optimization of the parameters describing the spectrographic part of NIRSpec, that is the instrument from the MSA to the FPA.

2.1 The reference data set

The main principle underlying the model optimization consists in adjusting the many model parameters to minimize the distance between the model-computed and the measured location of a set of spectral lines and aperture images (the reference data), in the NIRSpec main optical planes.

Because NIPS uses the transforms of the parametric model, the optimization of the model has to follow an iterative approach. So, the images and spectra from the calibration exposures are extracted from the count-rate images with an increasing level of accuracy in terms of wavelength and spatial location at the FPA, as one proceed through the various steps of the overall procedure for the model calibration. This involves a first, so called “manual adjustment” step, in which large differences between predicated and observed images and spectra location in the detector-arrays are adjusted by manually entering appropriate coordinate off-sets (e.g of the quadrants location) and a second step in which the model free parameters are simultaneously modified by a least square fit to yield the best agreement between the model-computed and the observed positions of the reference images and spectral lines.

For the optimization of the NIRSpec parametric model three types of data are necessary: imaging data, continuum spectra, and spectral lines. The first two sets provide spatial reference data, while the last one is used to derive spectral references. For the imaging mode, we acquired exposures of the MSA, illuminated by the CAA TEST lamp, in a checkerboard pattern. The imaging reference data comprise the positions of all fixed-slit plus a subset of the MOS aperture (roughly 6000).

For spatial reference of the grating modes, we used the CAA sources FLAT1, FLAT2, and FLAT3 that provide blackbody spectra for the three wavelength ranges $1.0 - 1.8$ μm, $1.7 - 3.0$ μm, and $2.9 - 5.0$ μm, matched to the NIRSpec bands. The spectral references are provided by the CAA sources REF, which is a rare earth absorption

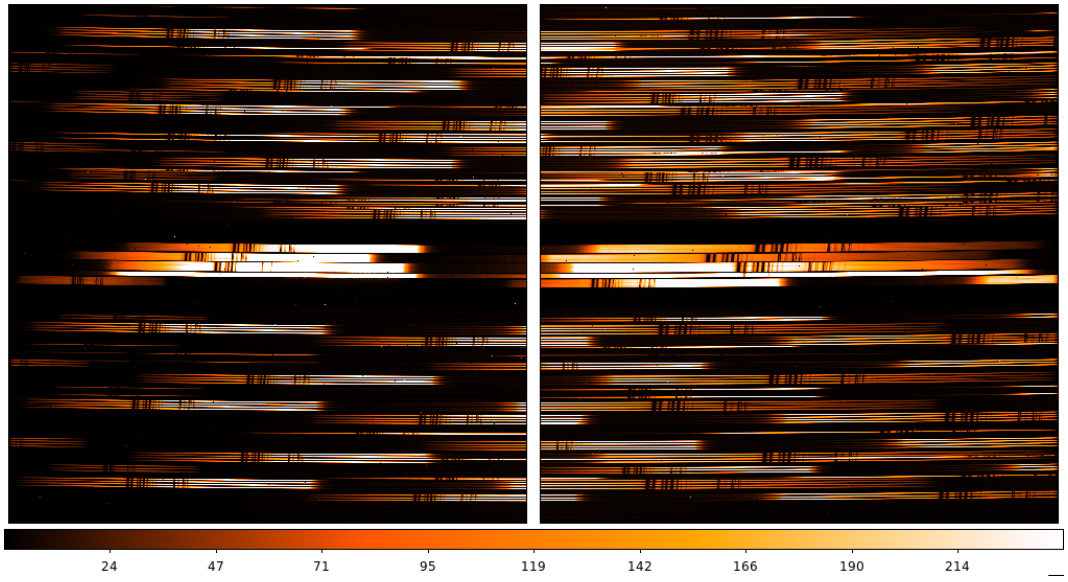

Figure 2: Count-rate images of the two NIRSpec detector arrays of an exposure of the REF lamp acquired with G395H (second and third order are visible) and the MSA configured in a dashed slit pattern. The regular pattern of spectra is spoiled by the missing spectra due to shutters that fail to open, or by misaligned, overlapping spectra from shutters that cannot be closed (stuck open). The image was generated from NIRSpec raw data using our pre-processing pipeline.

line source (Erbium) with absorption features in the $1.4 - 1.6$ μm wavelength range, and LINE1, LINE2 and LINE3, that employ Fabry-Perot type interferometric filters to provide five well defined transmission features over Band I, II, and III. All the CAA sources provide a spatially uniform illumination of the NIRSpec slit plane.

For each grating selection, 3 exposures with the MSA configured in a pattern of multiple dashed-slits were acquired, one illuminated by the continuum flat field lamp appropriate for that grating, the second set illuminated with the appropriate LINE lamp, and the third one using the REF lamp, in the gratings' second and third order for band II and III gratings. A so-called dashed-slit consists of 14 shutters in a column, where an open shutter is followed by a closed one, yielding seven open shutters per slit. Fig. 2 provides an image of REF spectra taken with the MSA dashed-slit pattern and grating G395H. For the prism we acquired exposures with LINE4 to cover the entire bandwidth using a MSA multiple dashed-slit configuration more densely packed than that for the gratings.

For each exposure, the count-rate images were derived from the raw exposure data using the pre-processing pipeline (Birkmann 2011) with default settings. This involves the following steps: bias subtraction, reference pixel subtraction, linearity correction, dark subtraction,[1] and up-the ramp fitting, as described in more detail in Birkmann (2011) and Böker et al. (2012). For the gratings, exposures of the LINE lamps where flat-fielded with the matching continuum exposures, for the prism data the detector flat-field was used.

Using NIPS, spectral traces from the fixed-slits and MSA microshutters were extracted from the count-rate images, rectified and collapsed to 1D-spectra (flux versus wavelength) computing the median along the spatial direction in each wavelength bin. Fig. 3 shows the spectra of REF and LINE1, as extracted from NIRSpec data. The centroid of the absorption and emission features of the CAA sources was computed from the 1D-spectra using the center of gravity (CoG) method (Cameron et al. 1982). The centroids of the spectral features are used to determine the x-position of the reference point at the FPA, while a polynomial fit to the flat field data is used to derive the corresponding y-position - see Dorner et al. (2016) for more details. At the end of this processing, the MOS spectral reference data sets comprise of the FPA positions for roughly 4,500 spectral lines

[1] Dark subtraction is carried out at the data cube level, i.e., the corresponding frame from a low-noise dark-currents cube is subtracted from each frame of the exposure.

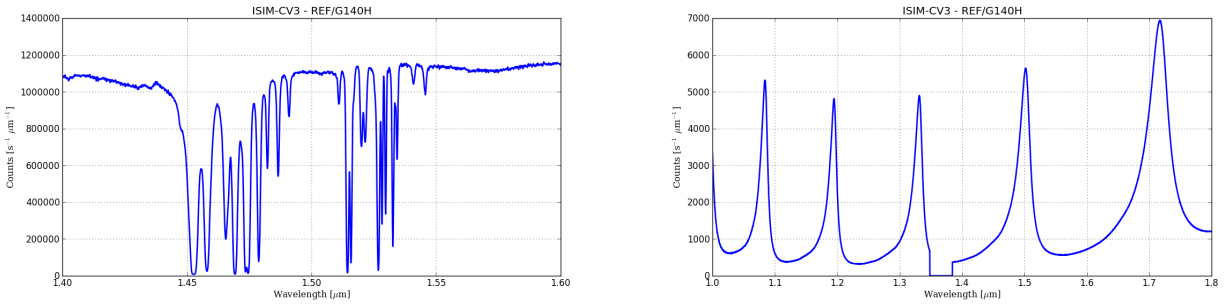

Figure 3: The spectra of two of the NIRSpec internal calibration sources REF (left) and LINES1 (right), taken with G140H. The Center of Gravity of the absorption and emission features of these sources were used as reference points for the optimization of the instrument's parametric model. No data are available for the spectrum of LINES1 around 1.35−1.38 μm, because in this range the light falls onto the gap between the two detectors (for this slit and grating combination).

for the gratings and 900 lines for the prism. IFU images and spectra of REF were also acquired, but, as we shall seen, only used for the verification step.

2.2 The model optimization

Because all the optical elements of NIRSpec are strongly pre-loaded and the structures of all the mirrors are made of Silicon-carbide (SiC), which is thermally very stable, there are no reasons to expect that the model representation of NIRSpec for the coordinate transforms and the internal geometry of the FPA elements should have changed between ISIM-CV3 and OTIS. So, after having collected all the reference points, we proceeded with the model optimization by least-square fit of a reduced set of the parameters, following the so called 'reduced optimization approach', as outlined in Giardino & Ferruit (2014).

The parameters for which changes are expected are the alignment angles of the dispersers and the mirror mounted on the GWA. Regarding the MSA, the array are isostatically mounted to the MSA cruciform structure, and small displacements in the quadrants positions and rotations can in principle be expected. Indeed when the 'reduced' approach was first validated against the data acquired during Cycle 2B of the Instrument Performance and Verification Campaign, the center and rotation of MSA Q1 had to be re-optimized compared to the values determined for Cycle 2A (Giardino & Ferruit 2014)[2].

The first step of the reduced approach consists in the optimization of the mirror tilt angle in x- and y-direction and, if necessary, the MSA quadrants location using the imaging data derived from the checkerboard exposure. Figure 4 shows the residuals between the measured and model predicted positions at the FPA for the micro-shutters centers after fitting only the two Mirror tilt angles. It is clear from the illustration that a pattern of significant residuals at the edge of all the quadrant is still present and the size of the standard deviation of the residuals in x and y (given in the figure) is about double the value that was achieved for ISIM-CV3 (Giardino & Lützgendorf 2016). Therefore we proceeded in performing a new fit, this time thawing the rotation angle and x- and y-coordinates of the quadrants centers, in addition to the two alignment angles of the mirror for a total of 14 free parameters $(12 + 2)$, for more than 5,500 data points.

The results of this second round of optimization can be seen in Fig. 5, the residuals are visually significantly smaller and the RMS of their distribution in spatial and dispersion direction is reduced to less than half what was achieved with only the two free parameters of the mirror. As listed in Table 1 the residuals RMS in the two orthogonal direction is less than 1/50 of a pixel, with values that are very similar to those achieved for CV3.

[2]Note that the detector performance at the time was significantly worse, so that small(er) displacements of the other quadrants may have gone undetected then

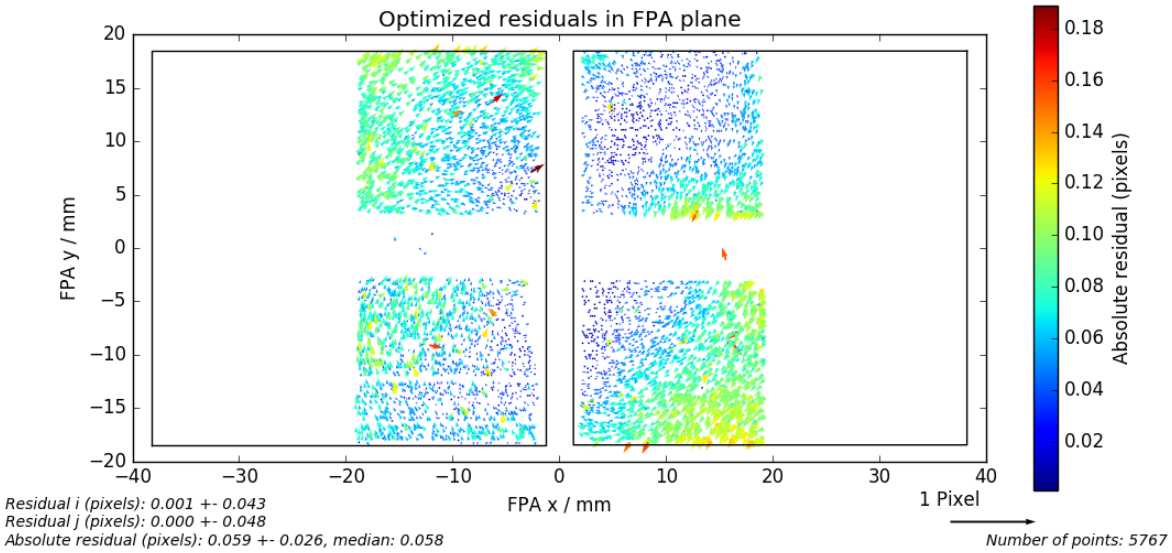

Figure 4: Residuals between the measured and model predicted positions at the FPA for the micro-shutters centers after optimizing only the two Mirror tilt angles.

Table 1: Residuals on the detectors of the optimized model forward projection MSA-to-FPA of the reference points for the MIRROR, all the gratings combined, and the prism. Here i is for dispersion direction and j for spatial direction.

GWA	Residual / pixels		
elements	i mean + RMS	j mean + RMS	median absolute
Mirror	0.000 ± 0.015	0.001 ± 0.019	0.019
Gratings	0.001 ± 0.084	0.000 ± 0.024	0.057
Prism	0.001 ± 0.126	0.001 ± 0.027	0.094

The new values of the alignment angles for the mirror are given in Table 2. Note that this angle is with respect to the plane defined by the mirror surface for the CV3 model, with respect to which the coordinate transforms and the FPA and MSA alignment had been optimized. Table 3 provides the new values of the 12 MSA parameters that were optimized, together with the difference with respect to the values assigned at CV3. All the quadrants appeared to have rotated by a 10 arcsec or so (clockwise), the adjustment in the center coordinates are of the order of a few micron or less. However, we note that to achieve a level of imaging residuals similar to that of CV3, these coordinate parameters had to be freed, or in other words fitting only the rotation angles was not sufficient to eliminate significant patterns in the residuals.

The next and last step of the reduced optimization approach consists in optimizing the tilt angles in X, Y and Z at the GWA of all the dispersers, using the spectral reference points. Unlike for the global optimization approach used for the CV3 calibration when MSA and FPA geometry, coordinates transforms of the collimator and camera and the orientation angles at the GWA of 4 out of 6 gratings (M-gratings plus G395H) are optimized simultaneously using the spectral reference data of the 4 gratings at once, in the reduced approach the alignment angles at the GWA are optimized for each disperser individually using the disperser's spectral data set. The new values for the dispersers orientation angles are given in Table 2, where they can be compared with those assigned for CV3. The plot of the distribution of the residuals between model-predicted and measure locations of the

Table 2: Optimized alignment tilt parameters of the mirror and the dispersers for the CV3 and the OTIS model, relative to the mirror surface at CV3.

GWA	Alignment tilt CV3/ arcsec			Alignment tilt OTIS/ arcsec		
Element	x	y	z	x	y	z
MIRROR	0.0	0.0	-	-5.6	37.1	-
G140H	114.5	1.3	-1599.8	111.2	17.5	-1591.4
G235H	87.0	-125.0	-1932.7	83.0	-113.7	-1921.4
G395H	82.9	-111.2	-1547.1	82.34	-86.14	-1541.43
G140M	130.0	60.0	-1520.2	126.4	80.7	-1506.0
G235M	125.5	153.0	-1495.2	124.07	176.49	-1491.5
G395M	211.7	44.9	-1572.2	207.8	66.21	-1569.2
PRISM	120.0	-911.70	-511.2	107.81	-992.02	-499.8

reference points at the FPA, for all the gratings, is shown in Fig. 6.

The histograms of the distribution of the residuals in dispersion and spatial direction at the FPA (respectively i and j) are given in Fig. 7. The results, in terms of mean and median of the residuals at the FPA in spatial and spectral direction, for all the modes are summarized in Table 1. The residuals are overall small, with a typical (median) amplitude less than 1/10 of a pixel for all the modes. Fig. 8 to Fig. 14 shows the residual distribution at the FPA for each individual disperser, including the prism.

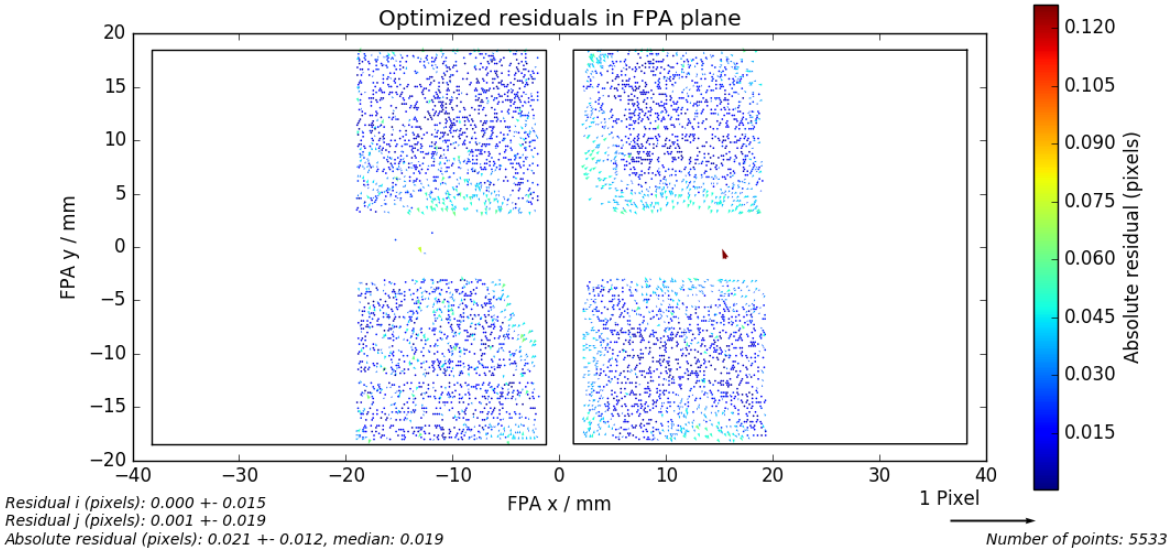

Figure 5: Residuals between the measured and model predicted positions at the FPA for the micro-shutters center after optimizing the two alignment angles of the mirror together with the location (x and y-coordinates of quadrant center) and rotation of each quadrant, corresponding to 12 additional parameters, for a total of 14 free parameters.

Table 3: MSA geometry: change in location and rotation of MSA quadrants from CV3 to OTIS

Center	CV3 / mm	OTIS / mm	difference / μm
Q1: X	-42.69	-42.69	0.99
Q1: Y	-41.85	-41.86	-3.86
Q2: X	-42.81	-42.81	-0.76
Q2: Y	7.27	7.26	-4.68
Q3: X	4.59	4.59	2.84
Q3: Y	-41.85	-41.86	-0.92
Q4: X	4.60	4.60	0.42
Q4: Y	7.26	7.26	-0.54

Rotation	arcsec	arcsec	arcsec
Q1	-74.81	-63.25	11.56
Q2	-51.96	-35.65	16.30
Q3	-35.54	-27.08	8.45
Q4	-31.43	-22.01	9.42

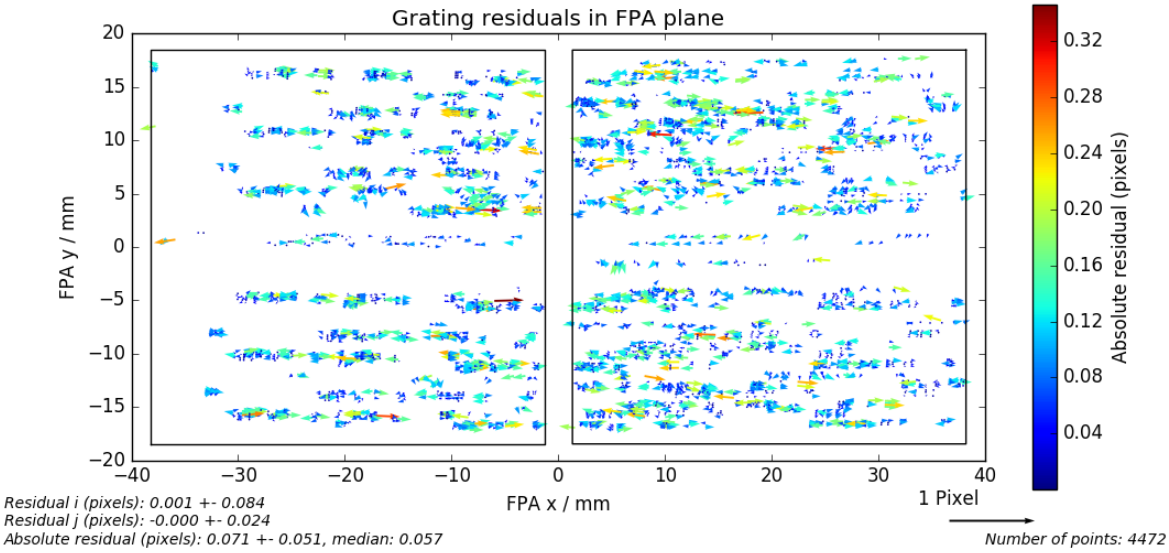

Figure 6: Residuals of forward coordinate transforms MSA-to-FPA, for all gratings on the detectors. The vectors give amplitude and direction of the difference between measured and model-computed location of the data points used to optimize 18 free parameters of the instrument model corresponding to the three tilt-angles for each grating.

3 RESULTS AND DISCUSSION

With the model optimized, one can now evaluate the accuracy of the model wavelength calibration by looking at the residuals between the "true" wavelength of the reference lines and their values as measured in NIRSpec spectra, extracted using NIPS, from the spectral traces of fixed-slits, MSA microshutters, or the IFU, for all the exposures acquired during the model calibration sequence at OTIS.

As for the initial step of generating the reference data, the traces were extracted from the count-rate images, rectified and collapsed to 1D-spectra (flux versus wavelength) computing the median along the spatial direction in each wavelength bin and rejecting the pixels flagged as 'dead' (by the pre-processing pipeline)[3]. The centroid of the absorption and emission features of the CAA sources was computed from the 1D-spectra using the center of gravity (CoG) method (Cameron et al. 1982) and the residuals of the calibration computed by taking the difference between the lines' center and their reference value. Since this process is fully automatic and the goodness of the individual CoG measures are not individually evaluated, at this point we rejects all CoG values that are more than a quarter of a resolution element away from their reference value (i.e residuals $> |0.5|$ pixel). Despite these rejections, for MOS, we were left with a number of lines going from the 675 for G235M to 1343 for G395H, the typical value being around 900. For the IFU the number of lines is typically around 200, while for the SLITS (`SLIT_A200_2`, `SLIT_A200_1` and `SLIT_B200`) the number are necessary small, but on the other hand we performed hardly any rejection.

The results are summarized in Table 4 for all the modes. The residuals (1-σ) RMS are at the level of 1/10 of a pixel for all the grating modes, corresponding to a wavelength calibration accuracy of $\sim$ 1/20 of a resolution element. This is two times better than the formal standard deviation allocation of 0.2 pixel (or 1/10 of a resolution element) specified for this step in the overall wavelength calibration budget of NIRSpec. For the prism, the model accuracy is at the level of a $\sim$ 1/14 of a resolution element, also within the requirements.

Table 4: Residuals between the 'true' wavelengths (CoGs) of the spectral features of the REF and LINES sources and those measured in the NIRSpec spectra extracted using the optimized parametric model (via NIPS). The values are average and RMS of the difference between the two quantities, over many lines, from MOS, fixed slit and IFU spectra, however for the IFU only the REF lines were used.

	Residual [pixel]			Residual [nm]		
Disperser	SLIT	MOS	IFU	SLIT	MOS	IFU
G140H	0.044 ± 0.072	0.009 ± 0.112	-0.012 ± 0.044	0.011 ± 0.018	0.000 ± 0.023	-0.004 ± 0.011
G235H	0.057 ± 0.088	0.012 ± 0.102	-0.008 ± 0.054	0.022 ± 0.035	0.002 ± 0.036	-0.029 ± 0.020
G395H	0.068 ± 0.078	0.017 ± 0.102	0.008 ± 0.093	0.045 ± 0.051	0.010 ± 0.066	0.005 ± 0.063
G140M	0.065 ± 0.100	0.026 ± 0.095	-0.004 ± 0.059	0.041 ± 0.064	0.007 ± 0.047	-0.026 ± 0.039
G235M	0.041 ± 0.058	0.020 ± 0.075	-0.068 ± 0.056	0.044 ± 0.062	0.011 ± 0.064	-0.076 ± 0.045
G395M	0.028 ± 0.051	0.006 ± 0.086	$-0.059 \pm 0.101^{\dagger}$	0.049 ± 0.092	0.003 ± 0.136	$-0.106 \pm 0.181^{\dagger}$
PRISM	0.028 ± 0.073	-0.004 ± 0.126	0.006 ± 0.155	0.535 ± 1.388	-0.069 ± 2.357	0.108 ± 2.870

† more aggressive cut of outliers ($> |0.25|$ pixel)

The model accuracy obtained in this work is very similar to the results of the first iteration of the model calibration that was performed by Dorner et al. (2016) and that performed by Giardino & Lützgendorf (2016) using the ISIM-CV3 data for NIRSpec in its actual (flight) configuration. Those results were obtained performing a global fit to more than 200 free parameters of the instrument model, while the calibration presented here was performed follwing an incremental approach with respet to the model obtained for CV3 (that is the 'reduced' approach), which entiles fitting the alignement angles at the GWA of the dispersers and the mirror plus the MSA paramters that are necessary to reach a level of imaging residuals similar to those obtained at CV3. We note that this method is so sensitive to the actual alignments of NIRSpec optical elements that we register displacements of a few micron in the positions of the quadrant arrays of the MSA.

[3]For the LINES spectra, pixels flagged as 'open', 'adjacent-to-open', and 'low-QE' were also rejected

The results presented here provide the necessary update to the parameters of the instrument model and quantify the intrinsic wavelength calibration accuracy of this new version of the model. The fact that we reach here similar level of accuracies as in the previous work is a confirmation of the reliability and robustness of this model-based method of calibrating NIRSpec. Importantly, these results also establish that the 'reduced' approach deliver accuracies similar to those achieved with a global fit and it is therefore a viable method to use when no major changes in the overall alignment of the instrument are expected.

The accuracy of the model for the spectrographic part of the instrument is a crucial part in the overall process of the NIRSpec wavelength calibration, but it is not the only part. There are two other important contributors to the overall wavelength calibration budget: the calibration of the spectrum shift caused by the finite repositioning accuracy of the grating wheel and the mixing of spatial and spectral information when our apertures are significantly larger than the size of the point-spread function (so-called slit effect). The calibration of the effect of the grating wheel-induced shift for the OTIS data is described in Alves de Oliveira (2017a,b).

Ultimately, for sky observations, the optical paths through the FORE elements of NIRSpec also have to be calibrated. This, however, has to be combined with the calibration of the telescope optics, thus it will be carried out once the instrument is in space, during the commissioning period. Using the data acquired from observations of an astrometric field in imaging mode, the parameters of the FORE transform for each filter element in combination with that for the OTE will be determined. This step will complete the spatial and spectral calibration of NIRSpec prior to the start of any scientific activity.

4 REFERENCES

Alves de Oliveira, C. 2017a, Calibration of the GWA position sensors for all dispersers for the NIRSpec/OTIS Cryo Vacuum testing campaign, NIRSpec Performance Report ESA-JWST-SCI-NRS-RP-2017-006, ESA/STScI

Alves de Oliveira, C. 2017b, Calibration of the GWA position sensors for the mirror for the NIRSpec/OTIS Cryo Vacuum testing campaign, NIRSpec Performance Report ESA-JWST-SCI-NRS-RP-2017-005, ESA/STScI

Birkmann, S. 2011, Description of the NIRSpec pre-processing pipeline, NIRSpec Technical Note NTN-2011-004, ESA/ESTEC

Birkmann, S. M., Ferruit, P., Böker, T., et al. 2012, in Society of Photo-Optical Instrumentation Engineers (SPIE) Conference Series, Vol. 8442, Society of Photo-Optical Instrumentation Engineers (SPIE) Conference Series, 3

Böker, T., Birkmann, S., de Marchi, G., et al. 2012, in Society of Photo-Optical Instrumentation Engineers (SPIE) Conference Series, Vol. 8442, Society of Photo-Optical Instrumentation Engineers (SPIE) Conference Series, 3

Cameron, D. G., Kauppinen, J. K., Moffatt, D. J., et al. 1982, Applied Spectroscopy, 36, 245

Dorner, B., Giardino, G., Ferruit, P., et al. 2016, A&A, 592, A113

Giardino, G. 2013, An introduction to the NIRSpec parametric model, NIRSpec Technical Note NTN-2013-011, ESA/ESTEC

Giardino, G. & Ferruit, P. 2014, The accuracy of NIRSpec wavelength calibrationb, NIRSpec Performance Report NPR-2014-004/ESA-JWST-RP-21134, ESA/ESTEC

Giardino, G., Luetzgendorf, N., Ferruit, P., et al. 2016, in Society of Photo-Optical Instrumentation Engineers (SPIE) Conference Series, Vol. 9904, Space Telescopes and Instrumentation 2016: Optical, Infrared, and Millimeter Wave, 990445

Giardino, G. & Lützgendorf, N. 2016, The spectral calibration of JWST/NIRSpec: accuracy of the instrument model for the ISIM-CV3 test cycle, NIRSpec Performance Report ESA-JWST-SCI-NRS-RP-2016-011, ESA/STScI

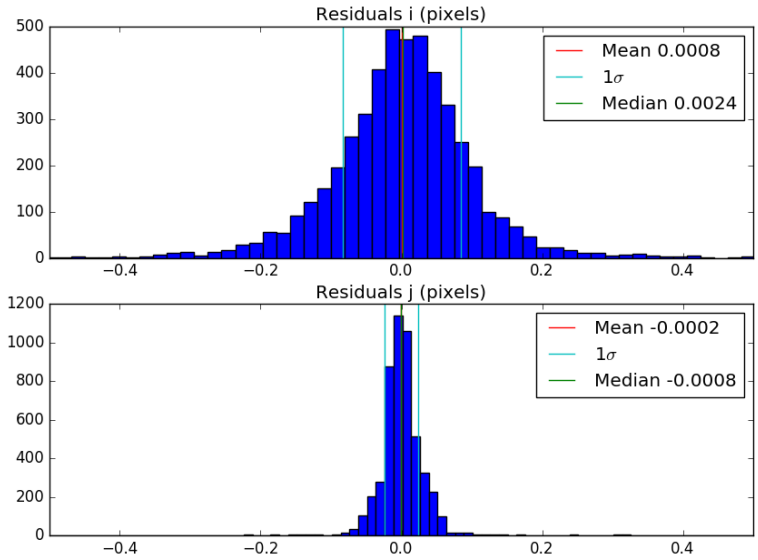

Figure 7: Distribution of the residuals of the forward coordinate transforms MSA-to-FPA after model optimization, for all the gratings, in i (dispersion) direction and j (spatial) direction (see text).

Kimble, R. A., Vila, M. B., Van Campen, J. M., et al. 2016, in Society of Photo-Optical Instrumentation Engineers (SPIE) Conference Series, Vol. This conference, Space Telescopes and Instrumentation 2016: Optical, Infrared, and Millimeter Wave

Rauscher, B. J., Boehm, N., Cagiano, S., et al. 2014, PASP, 126, 739

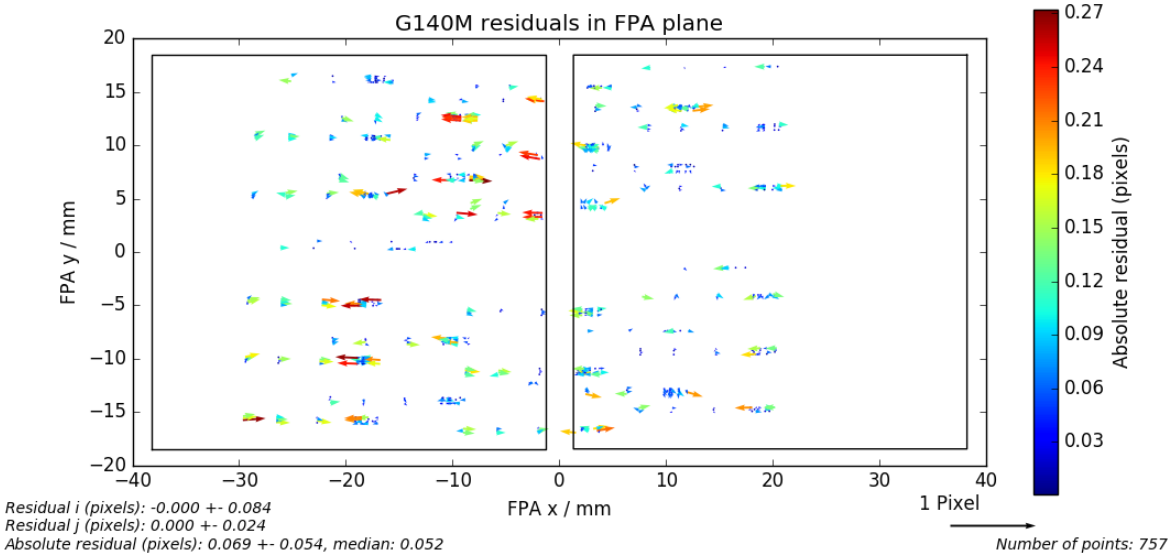

Figure 8: Residuals of forward coordinate transforms MSA-to-FPA, for G140M. The vectors give amplitude and direction of the difference between measured and model-computed location of the data points used to optimize the instrument model.

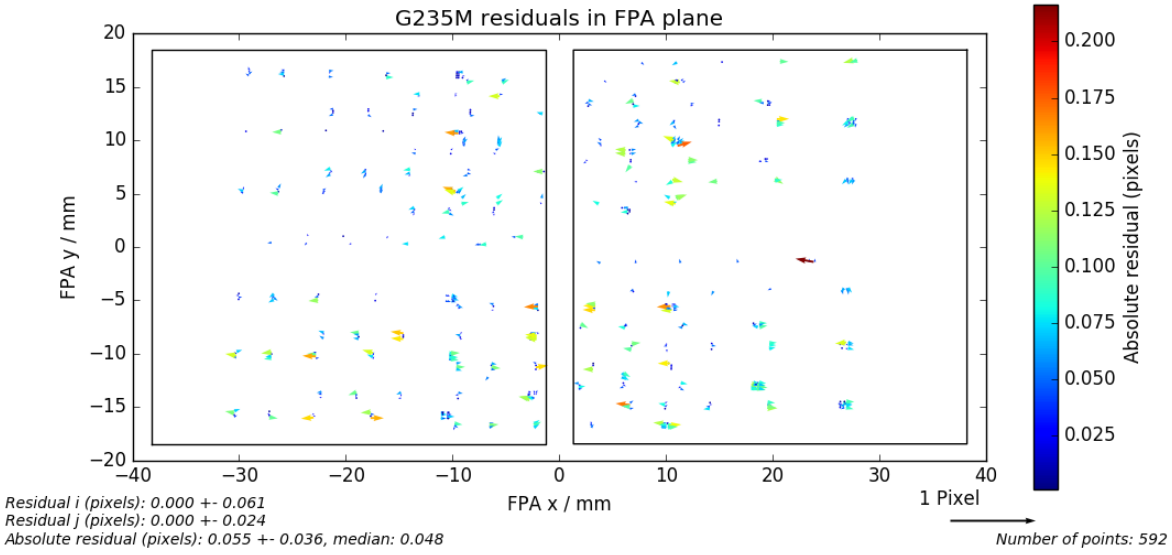

Figure 9: Same as Fig. 8 for G235M.

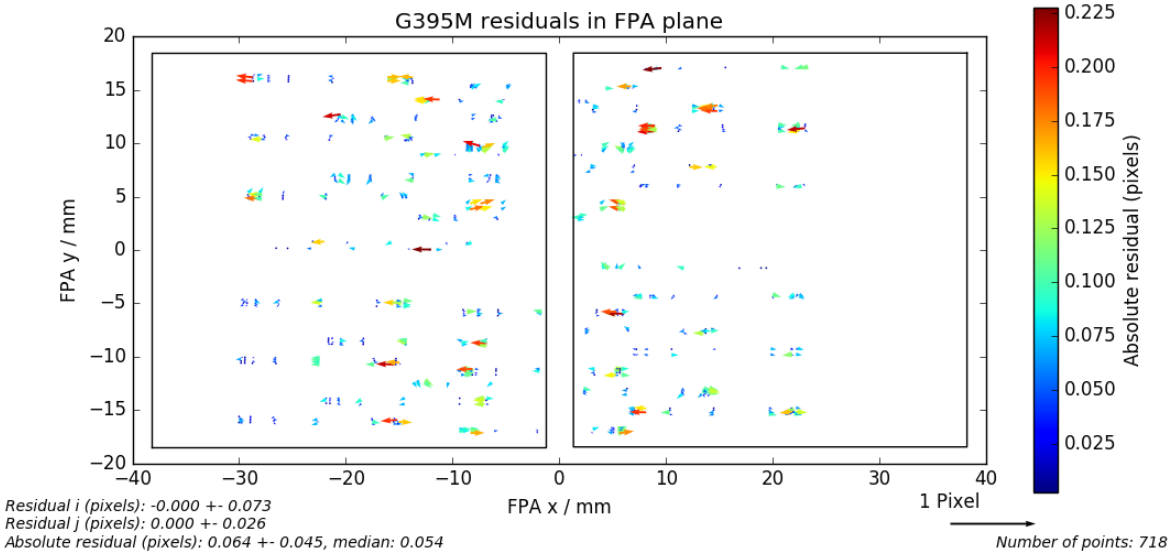

Figure 10: Same as Fig. 8 for G395M.

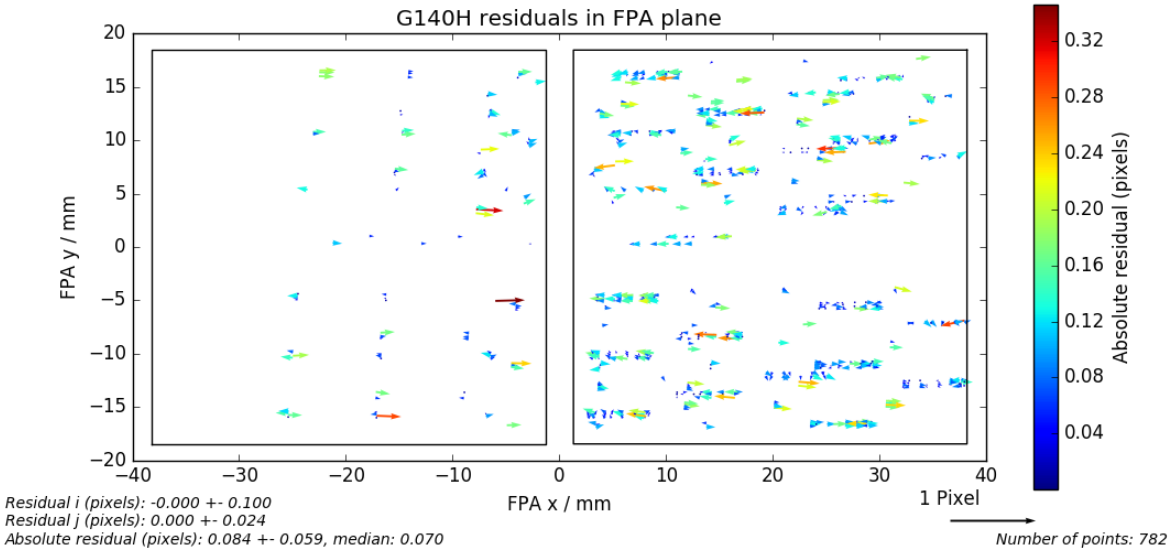

Figure 11: Same as Fig. 8 for G140H.

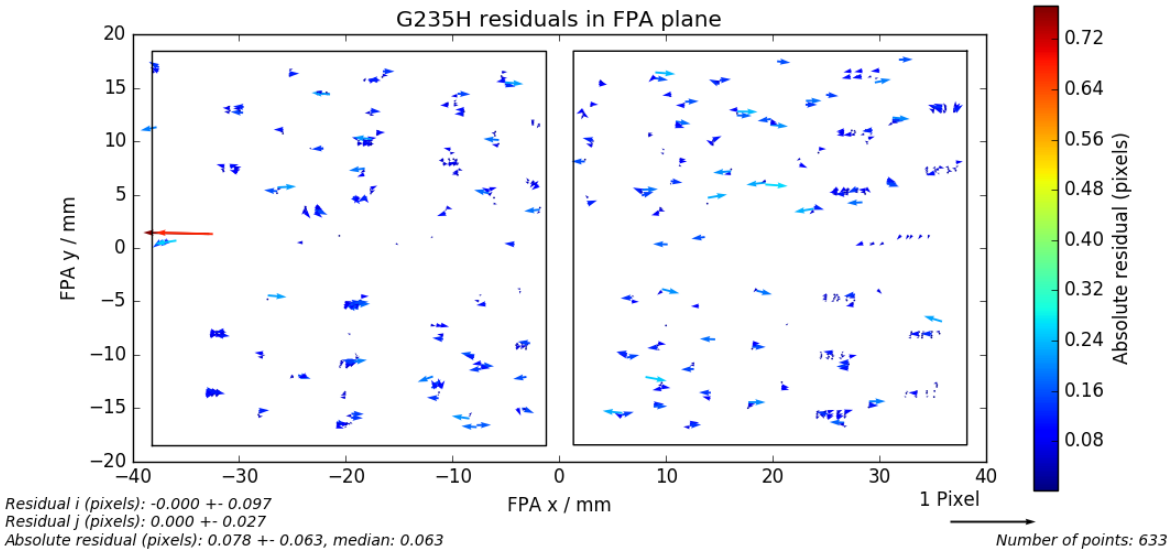

Figure 12: Same as Fig. 8 for G235H.

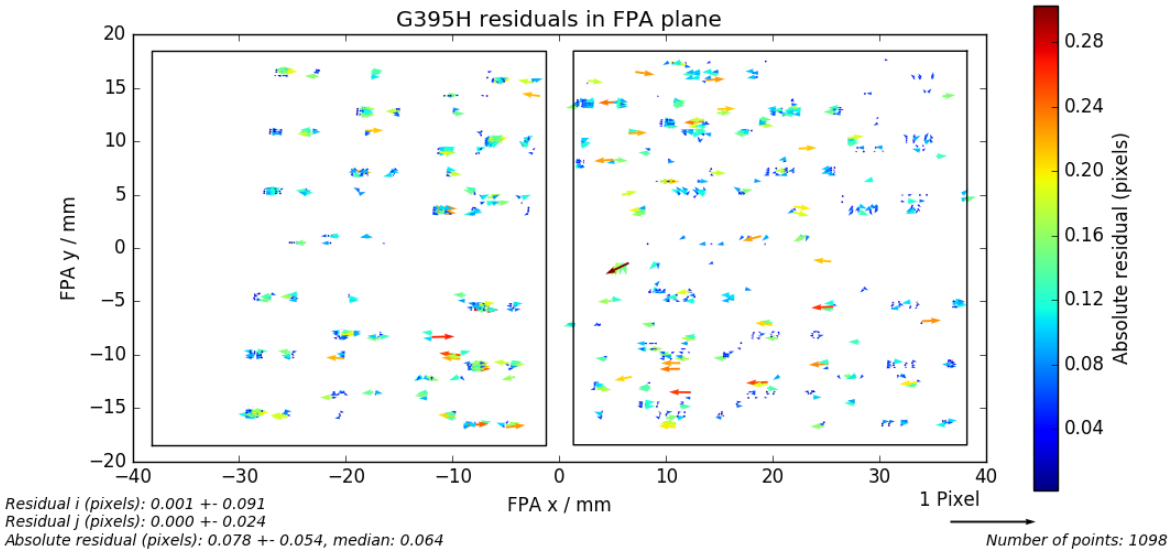

Figure 13: Same as Fig. 8 for G395H.

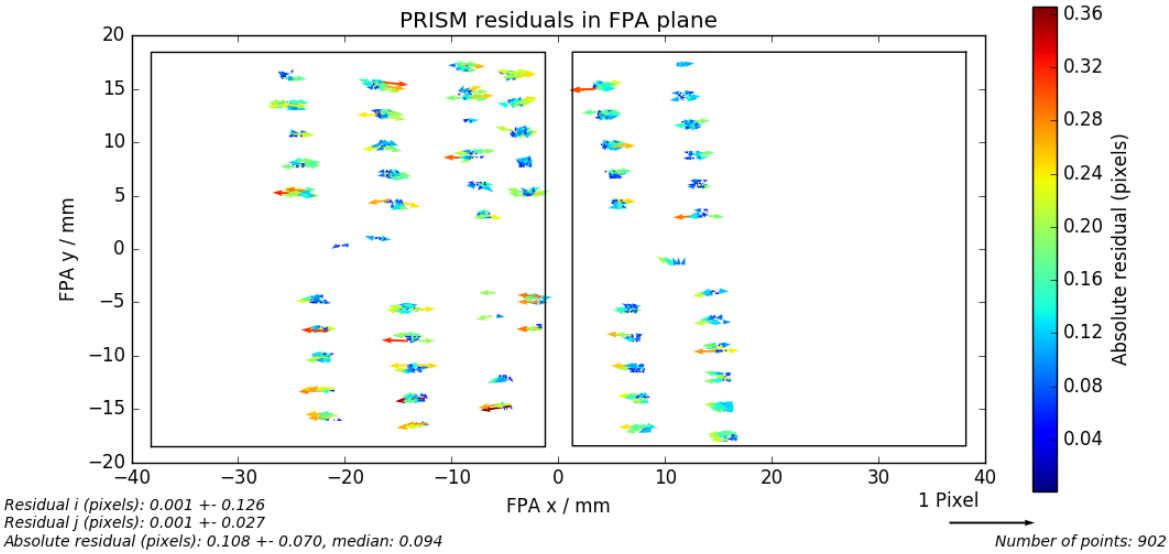

Figure 14: Same as Fig. 8 for the prism.